Title

Enantioselective Sulfonimidamide Acylation via a Cinchona Alkaloid-Catalyzed Desymmetrization: Scope, Data Science, and Mechanistic Investigation.

Journal

Journal of the American Chemical Society, 146(12)

Authors

Haas, Brittany

Lim, Ngiap-Kie

Jermaks, Janis

et al.

Publication Date

2024-03-27

DOI

10.1021/jacs.4c00374

Peer reviewed

HHS Public Access

Author manuscript

J Am Chem Soc. Author manuscript; available in PMC 2024 April 03.

Published in final edited form as:

J Am Chem Soc. 2024 March 27; 146(12): 8536–8546. doi:10.1021/jacs.4c00374.

Enantioselective Sulfonimidamide Acylation via a Cinchona Alkaloid-Catalyzed Desymmetrization: Scope, Data Science, and Mechanistic Investigation

Brittany C. Haas,
Department of Chemistry, University of Utah, Salt Lake City, Utah 84112, United States

Ngiap-Kie Lim,
Department of Synthetic Molecule Process Chemistry, Genentech, Inc., South San Francisco, California 94080, United States

Janis Jermaks,
Department of Synthetic Molecule Process Chemistry, Genentech, Inc., South San Francisco, California 94080, United States

Eden Gaster,
Department of Chemistry, Yale University, New Haven, Connecticut 06511, United States

Melody C. Guo,
Department of Chemistry, Yale University, New Haven, Connecticut 06511, United States

Thomas C. Malig,
Department of Synthetic Molecule Analytical Chemistry, Genentech, Inc., South San Francisco, California 94080, United States

Jacob Werth,
Department of Chemistry, University of Utah, Salt Lake City, Utah 84112, United States; Present Address: Chemical Research and Development, Pfizer Worldwide Research and Development, Groton Laboratories, Groton, Connecticut 06340, United States

Corresponding Authors: Ngiap-Kie Lim – Department of Synthetic Molecule Process Chemistry, Genentech, Inc., South San Francisco, California 94080, United States; lim.ngiapkie@gene.com; **Scott J. Miller** – Department of Chemistry, Yale University, New Haven, Connecticut 06511, United States; scott.miller@yale.edu; **Matthew S. Sigman** – Department of Chemistry, University of Utah, Salt Lake City, Utah 84112, United States; matt.sigman@utah.edu.

Author Contributions

All authors have given approval to the final version of the manuscript.

Supporting Information

The Supporting Information is available free of charge at https://pubs.acs.org/doi/10.1021/jacs.4c00374.

Cinchona catalyst and sulfonimidamide descriptors are provided in an Excel spreadsheet SI_Descriptors_P-CA_Modeling_Spreadsheet (XLSX)

Cinchona_catalysts_coordinates (XYZ)

Detailed experimental procedures, compound characterization data, kinetic analysis, computational methods, and an extended statistical modeling discussion are also available (PDF)

Accession Codes

CCDC 2271983 and 2323509–2323511 contain the supplementary crystallographic data for this paper. These data can be obtained free of charge via www.ccdc.cam.ac.uk/data_request/cif, or by emailing data_request@ccdc.cam.ac.uk, or by contacting The Cambridge Crystallographic Data Centre, 12 Union Road, Cambridge CB2 1EZ, UK; fax: +44 1223 336033.

Complete contact information is available at: https://pubs.acs.org/10.1021/jacs.4c00374

The authors declare no competing financial interest.

Haiming Zhang,
Department of Synthetic Molecule Process Chemistry, Genentech, Inc., South San Francisco, California 94080, United States

F. Dean Toste,
Department of Chemistry, University of California, Berkeley, California 94720, United States

Francis Gosselin,
Department of Synthetic Molecule Process Chemistry, Genentech, Inc., South San Francisco, California 94080, United States

Scott J. Miller,
Department of Chemistry, Yale University, New Haven, Connecticut 06511, United States

Matthew S. Sigman
Department of Chemistry, University of Utah, Salt Lake City, Utah 84112, United States

Abstract

Methods to access chiral sulfur(VI) pharmacophores are of interest in medicinal and synthetic chemistry. We report the desymmetrization of unprotected sulfonimidamides via asymmetric acylation with a cinchona-phosphinate catalyst. The desired products are formed in excellent yield and enantioselectivity with no observed bis-acylation. A data-science-driven approach to substrate scope evaluation was coupled to high throughput experimentation (HTE) to facilitate statistical modeling in order to inform mechanistic studies. Reaction kinetics, catalyst structural studies, and density functional theory (DFT) transition state analysis elucidated the turnover-limiting step to be the collapse of the tetrahedral intermediate and provided key insights into the catalyst-substrate structure–activity relationships responsible for the origin of the enantioselectivity. This study offers a reliable method for accessing enantioenriched sulfonimidamides to propel their application as pharmacophores and serves as an example of the mechanistic insight that can be gleaned from integrating data science and traditional physical organic techniques.

Graphical Abstract

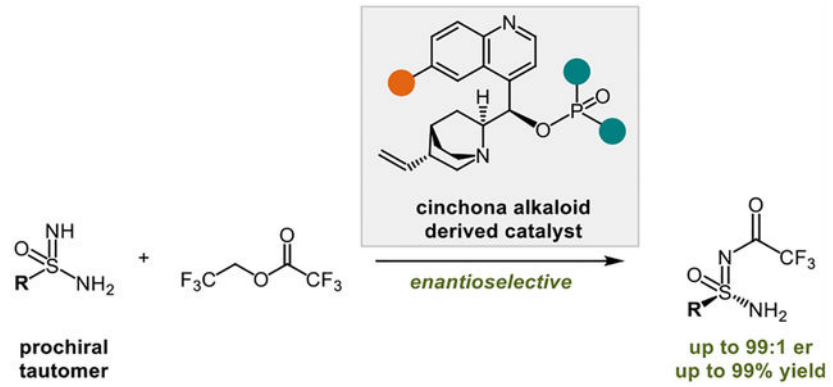

INTRODUCTION

Sulfur(VI) functional groups such as sulfonamides and sulfones have a rich history of impacting human life through medicinal and agrochemical applications. Their corresponding, largely untapped, chiral sulfur(VI) pharmacophores have recently emerged as targets of interest in medicinal chemistry.[1] As examples, sulfoximines,[2] sulfondiimines,[3] and sulfonimidamides[4] (Figure 1A) offer attractive properties for pharmaceutical applications: chirality, stability, solubility, desirable physicochemical characteristics, hydrogen bonding propensity, and multiple sites to incorporate structural diversity.[5] Specifically, sulfonimidamides have been postulated to be a chiral bioisostere to carboxylic acids[6] and sulfonamides,[7,8] common moieties in many drug candidates. However, this motif has yet to be widely deployed due to limited commercial availability and a dearth of practical asymmetric synthetic methods.

Willis and co-workers have reported an enantioselective alkylation of protected sulfonimidamides using cinchona alkaloid-derived phase-transfer catalysts.[9] Additionally, we have recently disclosed an enantioselective Pd-catalyzed aryl-carbonylation of sulfonimidamides with aryl and heteroaryl iodides (Figure 1B).[10] This reaction leveraged the rapid tautomerization of the imido and amido nitrogen atoms on unprotected sulfonimidamide starting materials, which provided a unique opportunity to desymmetrize the prochiral nitrogen atoms via dynamic kinetic resolution. With the desire to expand the number of enantioselective transformations and gain convenient access to the chiral sulfonimidamide pharmacophore, we investigated direct desymmetrization through acylation with a labile electrophile and a cinchona alkaloid for nucleophilic catalysis. This resolution of the two unprotected nitrogen nucleophiles on a single sulfur chiral center is challenging due to the tendency toward oligomerization and the lack of obvious structural differences required for effective catalyst recognition. Additionally, the nitrogens in both the starting material and monoacylated product are nucleophilic, which can result in competitive uncatalyzed reactions and the ability to form bis-acylated products (as observed in reported aryl-carbonylation reactions).[10,11] Related enantioselective acylation of nitrogen nucleophiles are sparse but include both enzymatic and small molecule catalysis, highlighted by independent efforts of the De and Seidel,[12] Fu and co-workers,[13] and Bode and co-workers[14] teams.

By combining chemical intuition and high throughput experimentation (HTE), we have identified an enantioselective acylation of unprotected sulfonimidamides to access enantiomerically enriched *N*-trifluoroacetyl-sulfonimidamides via cinchona-phosphinate catalysis (Figure 1C). Applying this unique catalyst scaffold[15] for an unreported reaction inspired a data science-informed evaluation of the substrate scope, which was leveraged to facilitate statistical modeling to drive traditional mechanistic studies. These investigations, which included reaction kinetics, catalyst structural studies, and density functional theory (DFT) transition state analysis, provided compelling evidence for the turnover-limiting collapse of the tetrahedral intermediate[16] and key insights into the origin of enantioselectivity.

RESULTS AND DISCUSSION

Discovery of the Active Catalyst and Optimization.

A preliminary exploration of an asymmetric *N*-acylation was performed on a model benzenesulfonimidamide substrate **1a** with 2,2,2-trifluoroethyl trifluoroacetate **2a** as the electrophile. Not only is **2a** commercially available but it was initially selected to provide a labile group to allow facile further functionalization (vide infra). Cinchona-based organocatalysts emerged as a promising class for this transformation. Derivatives consisting of ester, amide, sulfonamide, urea, thiourea, squaramide, and phosphorus-based functional groups were evaluated via HTE (Figure 2A) (see the SI for HTE details). Several of the cinchona derivatives demonstrated encouraging results in catalyzing this enantioselective transformation. The lead catalyst, furnishing the desired product **4aa**, was derived from a rarely utilized cinchona-phosphinate derivative.[15] Notably, this catalyst displayed excellent chemoselectivity, with no detectable bis-acylated product **5aa** observed. In contrast, bis-acylation was a competitive process for many of the other cinchona catalyst derivatives evaluated (up to 32% **5aa** observed in the crude reactions). Laboratory scale validation of catalyst **3a** confirmed the complete conversion of **1a** with no detectable amount of bis-acylated product **5aa** and high enantioselectivity of **4aa** (95:5 er) (Figure 2B). We hypothesized that the relationship between the basic, nucleophilic sites of the phosphinate catalyst **3** quinuclidine fragment, **1a**, and **2a** is key to the observed chemoselectivity. While we have not specifically evaluated the pK_a of the cinchona-phosphinate catalyst experimentally, calculations indicate that the pK_a of the amino group in **4aa** is lower by 1.6 units compared to starting sulfonimidamide **1a** (7.6 vs 9.2, respectively), making the second acylation leading to **5aa** more challenging.

We explored accessible phosphinate derivatives of the initial catalyst hit **3a** in an attempt to further improve the catalytic asymmetric reaction (Figure 2B). Electron-poor (**3b**), electron-rich (**3c**), and sterically hindered (**3d**) aryl derivatives did not influence the catalyst selectivity. Conversely, the relative substituent size of alkyl derivatives significantly impacted enantioselectivity (**3e**-**3g**, 69:31 to 96:4 er), with the optimal catalyst being the dicyclohexylphosphinate derivative **3e** (96:4 er). Modifications of the C6′-position on the quinoline fragment of **3a** were also evaluated. The protio derivative **3h** gave only moderate enantioselectivity (81:19 er) despite its distal location from the identified key phosphinate group. Installation of bulkier *i*-PrO or Ph substituents (**3i** and **3j**, respectively) had little impact on enantioselectivity (95:5 to 94:6 er, respectively). Two other aryl substituents gave unpredictable results, with the electron-withdrawing 3,5-bis(trifluoromethyl)phenyl substituent on catalyst **3k** adversely impacting selectivity (85:15 er), while little change to enantioselectivity was observed for electron-rich 4-methoxyphenyl derivative **3l** (94:6 er). Notably, the diversity of results coupled with the challenges in understanding the origin of selectivity provided the basis for the mechanistic analysis presented below.

Additional optimization of the reaction parameters, including temperature, concentration, catalyst loading, and electrophile equivalents, was pursued for the top-performing phosphinate catalyst **3e** (see the SI for details). Such changes to the standard reaction conditions reported in Figure 2B minimally affected enantioselectivity (93:7 to 97:3 er)

or conversion (>98%). Conversely, the solvent was found to impact the reaction (Figure 2B), as only moderate selectivity (76:24 to 80:20 er) was observed in nonethereal media, and reduced conversion (7%) was found in DCM. THF was determined to be the optimal solvent.

Substrate Scope.

We recently reported using chemical space visualization to qualitatively sample a diverse range of sulfonimidamide substrates, which was also deployed here (Figure 3B).[10] Examples were evaluated on bench-scale using the top-performing cinchona-phosphinate catalyst **3e** (Figure 3A). Exploration of the scope began by testing various substituted aryl sulfonimidamides. Different halogens placed at the *para*- (**1b**), *meta*- (**1c**), and *ortho*- (**1f**) positions afforded the corresponding acylated products **4ba** (98%, 96:4 er), **4ca** (71%, 99:1 er), and **4fa** (92%, 97:3 er) in high yields and excellent enantioselectivity. While 2-methylbenzenesulfo-nimidamide **1e** (87%, 94:6 er) reacted similarly to **1a**, increasing the electron density (**1d**, **1i**) and/or size of the aryl substituents (**1g, 1h**) resulted in a slight decrease in the enantioselectivity (81:19 to 92:8 er). Next, alkyl sulfonimidamides were tested under the reaction conditions. Benzyl sulfonimidamide **1j** reacted sluggishly with only moderate selectivity (55%, 67:33 er), whereas allyl **1k** (99%, 79:21 er) and cyclopropyl **1l** (98%, 91:9 er) substituted analogs afforded higher yields and improved enantioselectivity. The reaction was found to be compatible with various heteroaryl substrates such as pyridine **1m** (87%, 99:1 er), pyrimidine **1n** (89%, 99:1 er), furan **1o** (81%, 99:1 er), 5-chlorothiophene **1p** (95%, 99:1 er), and benzofuran **1q** (65%, 95:5 er). However, 7-chlorothieno[3,2-*b*]pyridine **1r** (14%, 96:4 er), benzothiazole **1s** (18%, 94:6 er), and 1-methylimidazole **1t** (7% conversion, 92:8 er) were formed in low yields, albeit with high enantioselectivity. Thus, these three substrates (**1r–1t**) were not included in subsequent HTE screening campaigns designed for statistical modeling to elucidate structure-enantioselectivity relationships (vide infra). Notably, no bis-acylated product was observed for any of the sulfonimidamide substrates tested. The absolute configuration of compounds **4aa, 4la, 4ma**, and **4qa** were determined to be (*S*) by single-crystal X-ray diffraction analysis.

Electrophile Scope.

The electrophile was also investigated using the optimized reaction conditions for **1a** with catalyst **3e** (Figure 4). Variations of the leaving group (purple sphere) were investigated and compared to the model electrophile 2,2,2-trifluoroethyl trifluoroacetate **2a**. Changing to the more electron-rich leaving group of ethyl trifluoroacetate **2b** resulted in no conversion, which is presumably due to the poorer leaving propensity of this group. Consistent with this observation, the reactivity is re-established upon incorporating a better-leaving group, *N*-trifluoroacetoxy succinimide (**2c**); however, this reaction resulted in no selectivity. Interestingly, selectivity correlates with leaving group ability, wherein phenyl trifluoroacetate **2d** and *S*-ethyl trifluoroethanethioate **2e** demonstrate modest improvements in the enantioselectivity. Additional electrophiles were also evaluated to explore the range of acyl groups that can be incorporated using this method (green sphere). The use of 2,2,2-trifluoroethyl difluoroacetate **2f** gave excellent selectivity (99:1 er) but with reduced

conversion (48%) compared to **2a**. More electron-rich electrophiles **2g, 2h, 2i**, and **2j** resulted in no conversion. Ultimately, 2,2,2-trifluoroethyl trifluoroacetate **2a** was determined to be the optimal electrophile for this transformation.

Applications of the Methodology.

To demonstrate the utility of this method, we prepared chiral sulfonimidamide analogs of the antitumor agent tasisulam[17–19] and the antiplatelet drug elinogrel[20] (Figure 5). Coupling **4pa** with 2,4-dichlorobenzoic acid **6** using a standard 1-[bis-(dimethylamino)methylene]-1*H*-1,2,3-triazolo[4,5-*b*]-pyridinium 3-oxide hexafluorophosphate (HATU)/*N*,*N*-diisopropylethylamine (DIPEA) protocol followed by TFA deprotection using ammonia produced the tasisulam-sulfonimidamide analog **7** in 74% yield with no erosion in enantioselectivity, demonstrating the stability of these sulfonimidamide products to a highly enabling reaction. The elinogrel-sulfonimidamide analog **9** was synthesized in a three-step, one-pot procedure. Substrate **4pa** was reacted with *p*-nitrophenyl chloroformate to produce the corresponding carbamate, which reacted with **8** to form unsymmetrical urea. Lastly, TFA deprotection gave the product in 42% yield and retained stereochemical integrity at 98:2 er.

Statistical Modeling for the Substrate–Catalyst Relationship.

Having evaluated the scope of the reaction using a singular catalyst, the nature of the structure-enantioselectivity relationship as it relates to both the substrate and catalyst was not obvious. We were especially interested in the role of the cinchona-phosphinate in catalyzing a highly enantioselective reaction for an unusual reactant. We deployed an arsenal of mechanistic and data-driven techniques to probe how the catalyst operates and what substrate features are required to achieve high enantioselectivity.

As the first stage, we designed an HTE screening campaign that assessed a combinatorial matrix of catalysts and substrates. The resultant quantity and diversity of data would allow for the construction of enantioselectivity correlations with substrate and catalyst structural features through statistical modeling.[21,22] By assessing a combinatorial matrix, we hypothesized that most general features required for effective asymmetric catalysis would be revealed and serve to seed further computational and mechanistic studies that are required to elucidate the mechanism of this reaction. Ten representative catalysts that sampled two points of modulation, the phosphinate and quinoline substituents, were selected as they showcased a diversity of responses in the initial optimization campaign. These catalysts were evaluated against the 17 sulfonimidamide substrates that provided reasonable yields in our initial scope evaluation (Figure 6A). The 170 reactions exhibited a well-distributed and wide range of observed selectivities ranging from 53:47 to 99:1 er, and 96% of the reactions achieved ≥85% conversion. The matrix approach highlights that each catalyst reacts uniquely with every substrate and vice versa, positioning this data set well for statistical modeling to decipher catalyst-substrate interactions that impact selectivity.

The data set was partitioned into three groups (Figure 6B). The first was an external validation set that was left out until the model building and selection were complete. This set included 17 data points (black boxes in Figure 6A, black stars in Figure 6C), representing

each substrate once and each catalyst once or twice. Of the remaining 153 data points, a Kennard Stone algorithm was used to define 50% as the training set (solid gray circles, Figure 6C) and the other 50% as the test set (teal crosses, Figure 6C). Forward-stepwise linear regression was employed to build models for the observed selectivity ($\Delta\Delta G^{\ddagger}$) using DFT-derived molecular descriptors of both the catalyst and the substrate.[21] Molecular mechanics conformational searches were used to generate conformer ensembles for both the substrates and the catalysts. After geometry optimization, each conformer's steric and electronic properties were collected to determine ensemble-dependent descriptors capturing molecular flexibility (see the SI for details).[23] The resultant models built from these descriptors were parsed based on their cross-validation and test-set statistical measures.[21] Averaged leave-one-substrate-out and leave-one-catalyst-out mean absolute error (MAE) values were used as an additional validation technique to ensure the model was not heavily biased to specific substrates or catalysts.[24] The presented model (Figure 6C) was selected to allow the descriptors and their coefficients to be interpreted to provide insight into the reaction mechanism; however, numerous models with similar statistics (presented in the SI) were determined. Averaged leave-one-substrate-out (0.224 kcal/mol) and leave-one-catalyst-out (0.223 kcal/mol) MAEs for this model indicate that in generalizing to the complete sampling of the substrate and catalyst members (training MAE = 0.185 kcal/mol), some precision is sacrificed. However, the external validation set was predicted similarly to the test set (test MAE = 0.177 kcal/mol, external validation MAE = 0.183 kcal/mol), demonstrating that the model can predict reactions of unseen substrate-catalyst combinations.

The four-parameter model consists of two terms for both the substrate and the catalyst. The natural bond orbital (NBO) partial charge of the substituent at the C6′-position on the quinoline classified the different substituents installed at this site (orange, Figure 6C). The more electron-rich (larger negative value) alkoxy-substituted catalysts give higher selectivities than the aryl or protio analogs. The buried volume collected within a 5 Å radius of C9 reads out the catalyst pocket established by the phosphinate substitution (red, Figure 6C). The larger buried volume provided by the cyclohexyl substituents (**3e**) restricts the pocket size, resulting in the most selective catalyst. The sulfonimidamide substrate is described by its molar volume (gray; Figure 6C). Although not independently correlated to the observed selectivity, we hypothesize that this parameter accounts for substrate-catalyst steric matching in the selectivity-determining transition state (vide infra). Lastly, the ^{13}C NMR chemical shift of the α-carbon (green, Figure 6C) serves to classify the aryl from the pseudoaliphatic (i.e., benzyl, allyl, and cyclopropyl) substrates, which exhibit lower selectivities.

Experimental Mechanistic Studies.

Having established quantitative structure-enantioselectivity relationships, we began kinetic investigations of the mechanism of catalysis to inform subsequent computational models. We selected in situ infrared (IR) spectroscopy as our analytical technique of choice to monitor the reaction's progress. Both the consumption of the starting electrophile **2a** and the formation of product **4aa** could be monitored via resolved peaks in the carbonyl region of the IR spectra (Figure 7A). From the outset of this study, we suspected that

an uncatalyzed background acylation reaction might play an impactful role in the process and be competitive with cinchona-catalyzed acylation. To gain further insight into the rate of the uncatalyzed background reaction, the reaction was performed and monitored in the absence of a catalyst (black, Figure 7B). A 10-fold difference in the initial rates was observed between the **3e**-catalyzed and uncatalyzed processes. Therefore, it is presumed that an aggregate rate of the cinchona-catalyzed reaction with a contribution from an uncatalyzed background reaction contributes to the reaction profile and observed selectivity. Importantly, precisely quantifying the exact background reaction contribution for each catalyst-substrate combination is challenging, but we estimate a ~5–30% background rate depending on the catalyst-substrate combination. This limits the selectivity ceiling to ~97:3 er for most examples.

Reaction progress kinetic analysis (RPKA)[25,26] and variable time normalization analysis (VTNA)[27] were performed on the reaction using catalyst **3e** and revealed a positive, near first-order dependence on the concentration of sulfonimidamide substrate **1a**, electrophile **2a**, and catalyst **3e**, allowing us to approximate the rate law as eq 1. The rate law is consistent with the formation of a ternary complex in the transition state.[28] However, due to the possible engagement of three different functional groups of the cinchona-phosphinate catalyst (i.e., phosphinate, quinuclidine, and/or quinoline groups) in contacts, we designed a set of experiments to elucidate the precise roles these fragments play in catalysis (Figure 7C).

$$\text{rate} \cong k[\text{sulfonimidamide}]^1[\text{electrophile}]^1[\text{catalyst}]^1 \quad (1)$$

Modifications to the phosphinate group of the top-performing cinchona-phosphinate catalyst **3e** demonstrated that substituting cyclohexyl with methyl substituents (**3g**) resulted in decreased enantioselectivity. This structural analog allowed us to compare with the thiophosphinate derivative **3m**, which resulted in a racemic product. This provides evidence that the phosphinate group is critical for selective catalysis. The next step was to differentiate the importance of basic nitrogens on the quinoline and quinuclidine sites. This was accomplished by selectively synthesizing the *N*-oxides at each nitrogen and sequentially determining how each impacts asymmetric catalysis. Excess *m*-CPBA in $CHCl_3$ was used to oxidize both nitrogen sites (**3p**), and compound **3o** was provided by subsequent selective quinuclidine *N*-oxide reduction ($NaHSO_3$, HCl/acetone), while oxidation using urea hydrogen peroxide in 2,2,2-trifluoroethanol afforded **3n** selectively. The quinuclidine *N*-oxide (**3n**) significantly impacted both the conversion and the enantioselectivity of the transformation; this was further confirmed by a similar result observed for the doubly blocked catalyst (**3p**). In contrast, the quinoline *N*-oxide (**3o**) did not impact the reaction outcome compared to the parent catalyst **3e**. This result was corroborated by kinetic experiments, where we observed a perfect overlay between the quinoline *N*-oxide (**3o**) and parent catalyst (**3e**) reaction profiles under standard reaction conditions (orange and teal, Figure 7B). These studies provided crucial insights into developing a computational model for asymmetric catalysis.

Computational Mechanistic Studies.

Once the quinuclidine and phosphinate fragments were determined as crucial for the success of the enantioselective reaction, catalyst-substrate complex structures were evaluated by docking the sulfonimidamide substrate in catalyst pockets proximate to the two groups. Choosing catalyst **3e** as a model catalyst, we found that the quinuclidine nitrogen and the phosphinate oxygen atoms can act as hydrogen-bond acceptors (Figure 8A). The cinchona-phosphinate catalyst efficiently forms doubly hydrogen-bound structures, anchoring the sulfonimidamide substrate (Figure 8B). During this binding event, we note that there does not seem to be any differentiation between imido versus amido nitrogen binding or preferential binding of one of the rapidly tautomerizing **1a** enantiomers.[29] We did, however, proceed with these structures as a starting point to evaluate the addition of 2,2,2-trifluoroethyl trifluoroacetate **2a**.

In light of our kinetic results, we extensively evaluated the direct addition of 2,2,2-trifluoroethyl trifluoroacetate **2a** to benzenesulfonimidamide **1a** as well as the subsequent collapse of tetrahedral intermediate **10aa** as the possible turnover limiting steps. Both scenarios fit the experimental rate law and agree with catalyst active site control experiments; thus, it is challenging to rule out one scenario conclusively over the other based purely on empirical data.

Using DFT calculations, we identified tetrahedral adduct transition state structures (*S*)-**11aa** and (*R*)-**11aa** and tetrahedral intermediate collapse transition state structures (*S*)-**12aa** and (*R*)-**12aa** that give access to enantiomers (*S*)-**4aa** and (*R*)-**4aa** (Figure 9).[30] We note that these structures were obtained after thorough consideration and a comprehensive search of all accessible conformers and rotamers for the aforementioned structures. The calculated addition and elimination transition state barriers ($\Delta G^{\ddagger}_{(\mathrm{add})}$ = 25.0 kcal/mol versus $\Delta G^{\ddagger}_{(\mathrm{col})}$ = 26.6 kcal/mol, respectively) should be surmountable under the reaction conditions. While both addition ($\Delta\Delta G^{\ddagger}_{(S)\mathrm{vs}(R)}$ = 1.4 kcal/mol) and elimination ($\Delta\Delta G^{\ddagger}_{(S)\mathrm{vs}(R)}$ = 1.4 kcal/mol) show a slight preference for the observed (*S*)-enantiomer, the energy barrier for the tetrahedral collapse is higher by $\Delta\Delta G^{\ddagger}_{(\mathrm{add})\mathrm{vs}(\mathrm{col})}$ = 1.6 kcal/mol. At this point, we address that upon the addition of the electrophile, a second stereocenter is generated in the tetrahedral adduct. For instance, starting material (*S*)-**1a** reacting with electrophile **2a** could form two tetrahedral adducts **10aa** with (*S, R*) and (*S, S*) configurations for the sulfur and carbon centers, respectively. However, only the (*S, R*)-adduct is accommodated in the tetrahedral collapse transition state (***S***)-**12aa** due to formation of a 6-membered ring intermediate and proper alignment of the trifluoroethoxy group for elimination by proton transfer from quinuclidine. We suspect that the tetrahedral adduct formation is reversible, and thus the other (*S, S*)-adduct can revert to starting materials that eventually proceed through the collapse transition state (*S*)-**12aa**. Furthermore, the necessity to have a good leaving group seems to be in accordance with our electrophile scope evaluation. Thus, we conclude that the collapse of the tetrahedral intermediate is most likely the rate- and selectivity-determining step.

Stereochemical Model.

Having used statistical modeling, reaction kinetics, catalyst structural studies, and DFT calculations as complementary tools to interrogate this transformation, a stereochemical model can be proposed. According to our mechanistic model, the sulfonimidamide substituent is placed pseudoequatorially in the 6-membered ring transition state leading to the preferred (*S*)-enantiomer. Smaller substrates in the transition state will have a lower preference for the sulfonimidamide substituent being placed pseudoequatorially versus pseudoaxially ((*S*)-**12**, Figure 10A), leading to selectivity erosion. However, larger substrates in the preferred pseudoequatorial position will lead to unfavorable steric interactions with the phosphinate substituents ((*R*)-**12**, Figure 10A). To identify substrates for which it is difficult for the catalyst to impart selectivity, we further investigated the steric terms in the original statistical model (Figure 6C). We plotted the substrate volume against the catalyst buried volume and overlaid the measured $\Delta\Delta G^{\ddagger}$ as a heatmap (Figure 10B). It confirms that the catalyst pocket is not amenable to small (<1000 Bohr radius^3/mol; **1k** and **1l**) nor large (>1490 Bohr radius^3/mol; **1i, 1g, 1h, 1q, 1j**) substrates.

The initial statistical model was trained on the observed selectivity (i.e., aggregate catalyst and background selectivity); however, subsequent kinetic studies highlighted the non-innocence of the background uncatalyzed reaction. We thus hypothesized that our initial model (Figure 6C) for the observed selectivity may have suffered from competing processes. To better understand the interplay of the catalyst and substrate steric matching required for enantioinduction and determine which catalysts and/or substrates may be most impacted by higher background reactivity, we further analyzed the steric heatmap (Figure 10B). There is a clear optimal region (gray-shaded area). The catalyst active region excludes catalyst **3g**, which contains the methyl-substituted phosphinate substituent. This observation can be explained by the fact that catalyst **3g** exhibits higher conformational flexibility seen in cinchona-derived catalysts[31–34] and is able to accommodate the substrate in various orientations (Figure 10C). The small methyl substituents are sterically less encumbered and allow for facile quinoline rotation in the catalyst, which leads to a faster reaction rate (green; Figure 10E). Additionally, the collapse of (*R*)-enantiomer tetrahedral intermediates having the sulfonimidamide substituents pseudoequatorially can be more readily accessed by catalyst **3g** ((*R*)-**14**, Figure 10C), which leads to degraded selectivity. The behavior of catalysts **3k** and **3h** (light purple shaded area, Figure 10B) is similar to those in the optimal region. However, the significant perturbation of the quinoline group (3,5-$(CF_3)_2C_6H_3$) for catalyst **3k** impacts the lowest ground state conformation of the catalyst (Figure 10D). To minimize the molecule's overall dipole, catalyst **3k** prefers to have the quinoline positioned orthogonally to the catalysts in the optimal region, thus lowering the ground state by ~1.0 kcal/mol. As a result, the overall activation barrier to the tetrahedral adduct collapse is increased (transition state analysis for catalyst **3h**, as well as for **3g** and **3k**, is provided in the SI), and the uncatalyzed background reaction becomes more competitive (purple, Figure 10E). Catalyst **3h** lies in some degree between catalysts **3g** and **3k**, as the erosion of the er is observed due to a combination of conformational flexibility, lower ground state energy, and slower rate (orange, Figure 10E).

With evidence that catalysts **3g**, **3h**, and **3k** proceed via alternative modes of action, we hypothesized a more robust statistical model could be constructed that better describes the primary mode of enantioinduction if these three catalysts were removed from the data set. It is probable that removing catalysts that are slower and have a more competitive uncatalyzed rate can serve to reduce the noise in the modeled selectivity data (i.e., observed selectivity would be more indicative of innate catalyst selectivity). The best four-parameter model consisted of one catalyst term and three substrate terms (Figure 10F). The model is substrate-dominated, with a notable catalyst term (average Sterimol L, teal, Figure 10F) that reads out substitution of both the phosphinate and quinoline C6′-position. The substrate molar volume (gray, Figure 10F) remains a model parameter, in addition to the Sterimol B_1 value (purple, Figure 10F) and buried volume within a 2.5 Å radius of the α-carbon (green, Figure 10F). The sulfonimidamide substrate parameters serve to describe the nature of the substrate in the catalyst pocket, for which the substrate must provide enough steric bulk to secure its conformation for enantioinduction. Although all the statistical measures of this model improve compared to the model trained on the full data set (Figure 6C), of significance is the increased precision (~0.1 kcal/mol) of the model in leave-one-substrate-out (MAE = 0.125 kcal/mol) and leave-one-catalyst-out (MAE = 0.132 kcal/mol) analysis.

CONCLUSIONS

An extensive experimental and computational analysis of this cinchona-phosphinate-catalyzed chemospecific acylation of sulfonimidamides was conducted. A data science-informed substrate and catalyst scope evaluation allowed for statistical modeling to inform traditional physical organic mechanistic studies, including reaction kinetics, catalyst structural studies, and DFT transition state analysis. The catalyst “active site” was mapped by deconstructing the important model parameters in conjunction with insight from these traditional physical organic techniques. We have developed a comprehensive understanding of the catalyst-substrate structure–activity relationship that accounts for the selectivity of this reaction and conclude the dicyclohexylphosphinate-cinchona alkaloid catalyst **3e** was robust for most sulfonimidamide substrates. Ultimately, the enantioselectivity determining event was proposed to be the collapse of the tetrahedral intermediate, which is often hypothesized for enzymatic processes,[35] not small molecule catalysis. This should provide inspiration for the development of related reactions involving the use of chiral sulfur(VI) pharmacophores. Additionally, this study highlights how data science tools can be merged with traditional physical organic methods in the pursuit of mechanistic analysis.

Supplementary Material

Refer to Web version on PubMed Central for supplementary material.

ACKNOWLEDGMENTS

We thank Dr. David Russell, Dr. Jose Napolitano, Dr. Yuhui Zhou, Dr. Chris Crittenden, and Dr. Sean Treacy for analytical support; Adam Childs for performing high-throughput experimentation; Dr. Antonio DiPasquale for X-ray crystallographic support; Kyle Clagg, Phillip Crook, Dr. Jordan Dotson, Dr. Kyle Mack, Dr. Jacob Timmerman, Dr. Kenji Kurita, and Jordan Liles for helpful discussions. Research in the Sigman group was partially supported by the NIH (R35 GM136271). The Center for High-Performance Computing supported the statistical modeling work at the University of Utah. Research in the Miller group was partially supported by the NIH (NIGMS

R35 132092). The Toste group acknowledges the support of the NIH (R35 GM118190). E.G. was supported in part by the Zuckerman STEM Leadership Program. M.C.G. was supported in part by the National Science Foundation Graduate Research Fellowship (DGE 2139841).

REFERENCES

(1). Tilby MJ; Willis MC How do we address neglected sulfur pharmacophores in drug discovery? Expert Opin. Drug Discovery 2021, 16, 1227–1231.

(2). Foote KM; Nissink JWM; McGuire T; Turner P; Guichard S; Yates JWT; Lau A; Blades K; Heathcote D; Odedra R; Wilkinson G; Wilson Z; Wood CM; Jewsbury PJ Discovery and Characterization of AZD6738, a Potent Inhibitor of Ataxia Telangiectasia Mutated and Rad3 Related (ATR) Kinase with Application as an Anticancer Agent. J. Med. Chem 2018, 61, 9889–9907. [PubMed: 30346772]

(3). Lücking U; Kosemund D; Böhnke N; Lienau P; Siemeister G; Denner K; Bohlmann R; Briem H; Terebesi I; Bömer U; Schäfer M; Ince S; Mumberg D; Scholz A; Izumi R; Hwang S; von Nussbaum F Changing for the Better: Discovery of the Highly Potent and Selective CDK9 Inhibitor VIP152 Suitable for Once Weekly Intravenous Dosing for the Treatment of Cancer. J. Med. Chem 2021, 64, 11651–11674. [PubMed: 34264057]

(4). Zhao P; Zeng Q Progress in the Enantioselective Synthesis of Sulfur (VI) Compounds. Chem. – Eur. J 2023, 29, No. e202302059.

(5). Lücking U Neglected sulfur(vi) pharmacophores in drug discovery: exploration of novel chemical space by the interplay of drug design and method development. Org. Chem. Front 2019, 6, 1319–1324.

(6). Borhade SR; Svensson R; Brandt P; Artursson P; Arvidsson PI; Sandström A Preclinical Characterization of Acyl Sulfonimidamides: Potential Carboxylic Acid Bioisosteres with Tunable Properties. ChemMedChem. 2015, 10, 455–460. [PubMed: 25630705]

(7). Chinthakindi PK; Naicker T; Thota N; Govender T; Kruger HG; Arvidsson PI Sulfonimidamides in Medicinal and Agricultural Chemistry. Angew. Chem., Int. Ed 2017, 56, 4100–4109.

(8). Zhang Z-X; Willis MC Crafting chemical space with sulfur functional groups. Trends Chem. 2023, 5, 3–6.

(9). Tilby MJ; Dewez DF; Hall A; Martínez Lamenca C; Willis MC Exploiting Configurational Lability in Aza-Sulfur Compounds for the Organocatalytic Enantioselective Synthesis of Sulfonimidamides. Angew. Chem., Int. Ed 2021, 60, 25680–25687.

(10). van Dijk L; Haas BC; Lim N-K; Clagg K; Dotson JJ; Treacy SM; Piechowicz KA; Roytman VA; Zhang H; Toste FD; Miller SJ; Gosselin F; Sigman MS Data Science-Enabled Palladium-Catalyzed Enantioselective Aryl-Carbonylation of Sulfonimidamides. J. Am. Chem. Soc 2023, 145, 20959–20967. [PubMed: 37656964]

(11). Recent work from Shaw and co-workers employed this desymmetrization strategy on heterocyclic sulfonimidamides to eliminate bis-functionalization concerns.Gutierrez D; Toth-Williams G; Yasuda M; Di Maso M; Shaw J Desymmetrization of Heterocyclic Sulfonimidamides via Asymmetric Tsuji-Trost Asymmetric Alkylation. ChemRxiv (catalysis). 2023-08-28, DOI: 10.26434/chemrxiv-2023-vx0fb (accessed 2023-12-14).

(12). De CK; Seidel D Catalytic Enantioselective Desymmetrization of *meso*-Diamines: A Dual Small-Molecule Catalysis Approach. J. Am. Chem. Soc 2011, 133, 14538–14541. [PubMed: 21863902]

(13). Arai S; Bellemin-Laponnaz S; Fu GC Kinetic Resolution of Amines by a Nonenzymatic Acylation Catalyst. Angew. Chem., Int. Ed 2001, 40, 234–236.

(14). Binanzer M; Hsieh S-Y; Bode JW Catalytic Kinetic Resolution of Cyclic Secondary Amines. J. Am. Chem. Soc 2011, 133, 19698–19701. [PubMed: 22082205]

(15). Sobhani S; Fielenbach D; Marigo M; Wabnitz TC; Jørgensen KA Direct Organocatalytic Asymmetric α-Sulfenylation of Activated C–H Bonds in Lactones, Lactams, and β-Dicarbonyl Compounds. Chem. – Eur. J 2005, 11, 5689–5694. [PubMed: 16035005]

(16). Menger FM; Smith JH Rate-determining collapse of a tetrahedral intermediate in ester aminolyses in aprotic solvents. Tetrahedron Lett. 1970, 11, 4163–4168.

(17). Simon GR; Ilaria RL; Sovak MA; Williams CC; Haura EB; Cleverly AL; Sykes AK; Wagner MM; de Alwis DP; Slapak CA; Miller MA; Spriggs DR A phase I study of tasisulam sodium

(LY573636 sodium), a novel anticancer compound in patients with refractory solid tumors. Cancer Chemother. Pharmacol 2011, 68, 1233–1241. [PubMed: 21431416]

(18). Gordon MS; Ilaria R; de Alwis DP; Mendelson DS; McKane S; Wagner MM; Look KY; LoRusso PM A phase I study of tasisulam sodium (LY573636 sodium), a novel anticancer compound, administered as a 24-h continuous infusion in patients with advanced solid tumors. Cancer Chemother. Pharmacol 2013, 71, 21–27. [PubMed: 23228983]

(19). Steinkamp A-D; Schmitt L; Chen X; Fietkau K; Heise R; Baron JM; Bolm C Synthesis of a Sulfonimidamide-Based Analog of Tasisulam and Its Biological Evaluation in the Melanoma Cell Lines SKMel23 and A375. Skin Pharmacol Physiol. 2017, 29, 281–290.

(20). Siller-Matula JM; Krumphuber J; Jilma B Pharmacokinetic, pharmacodynamic and clinical profile of novel antiplatelet drugs targeting vascular diseases. Br. J. Pharmacol 2010, 159, 502–517. [PubMed: 20050853]

(21). Santiago CB; Guo J-Y; Sigman MS Predictive and mechanistic multivariate linear regression models for reaction development. Chem. Sci 2018, 9, 2398–2412. [PubMed: 29719711]

(22). Raghavan P; Haas BC; Ruos ME; Schleinitz J; Doyle AG; Reisman SE; Sigman MS; Coley CW Dataset Design for Building Models of Chemical Reactivity. ACS Cent. Sci 2023, 9, 2196–2204. [PubMed: 38161380]

(23). Gensch T; dos Passos Gomes G; Friederich P; Peters E; Gaudin T; Pollice R; Jorner K; Nigam A; Lindner-D'Addario M; Sigman MS; Aspuru-Guzik A A Comprehensive Discovery Platform for Organophosphorus Ligands for Catalysis. J. Am. Chem. Soc 2022, 144, 1205–1217. [PubMed: 35020383]

(24). Reid JP; Sigman MS Holistic prediction of enantioselectivity in asymmetric catalysis. Nature 2019, 571, 343–348. [PubMed: 31316193]

(25). Blackmond DG Reaction Progress Kinetic Analysis: A Powerful Methodology for Mechanistic Studies of Complex Catalytic Reactions. Angew. Chem., Int. Ed 2005, 44, 4302–4320.

(26). Blackmond DG Kinetic Profiling of Catalytic Organic Reactions as a Mechanistic Tool. J. Am. Chem. Soc 2015, 137, 10852–10866. [PubMed: 26285166]

(27). Burés J Variable Time Normalization Analysis: General Graphical Elucidation of Reaction Orders from Concentration Profiles. Angew. Chem., Int. Ed 2016, 55, 16084–16087.

(28). Salehi Marzijarani N; Lam Y-H; Wang X; Klapars A; Qi J; Song Z; Sherry BD; Liu Z; Ji Y New Mechanism for Cinchona Alkaloid-Catalysis Allows for an Efficient Thiophosphorylation Reaction. J. Am. Chem. Soc 2020, 142, 20021–20029. [PubMed: 33180475]

(29). The calculated experimental activation barrier for the tautomerization process is ~10 kcal/mol. The activation energy barrier was determined through variable temperature ^{1}H NMR spectroscopy, with the maximum peak separation under slow-exchange limit determined to be 1200 Hz and the coalescence temperature estimated to be 233 K.

(30). In the following discussion, the (*S*) and (*R*) absolute configuration is specifically referring to the sulfur chiral center unless otherwise specified.

(31). Dijkstra GDH; Kellogg RM; Wynberg H; Svendsen JS; Marko I; Sharpless KB Conformational study of cinchona alkaloids. A combined NMR, molecular mechanics and x-ray approach. J. Am. Chem. Soc 1989, 111, 8069–8076.

(32). Bürgi T; Baiker A Conformational Behavior of Cinchonidine in Different Solvents: A Combined NMR and ab Initio Investigation. J. Am. Chem. Soc 1998, 120, 12920–12926.

(33). Olsen RA; Borchardt D; Mink L; Agarwal A; Mueller LJ; Zaera F Effect of Protonation on the Conformation of Cinchonidine. J. Am. Chem. Soc 2006, 128, 15594–15595. [PubMed: 17147361]

(34). Molchanov S; Rowicki T; Gryff-Keller A; Koźmiński W Conformational Equilibrium of Cinchonidine in C_6D_{12} Solution. Alternative NMR/DFT Approach. J. Phys. Chem. A 2018, 122, 7832–7841. [PubMed: 30240224]

(35). Kazemi M; Sheng X; Kroutil W; Himo F Computational Study of Mycobacterium smegmatis Acyl Transferase Reaction Mechanism and Specificity. ACS Catal. 2018, 8, 10698–10706.

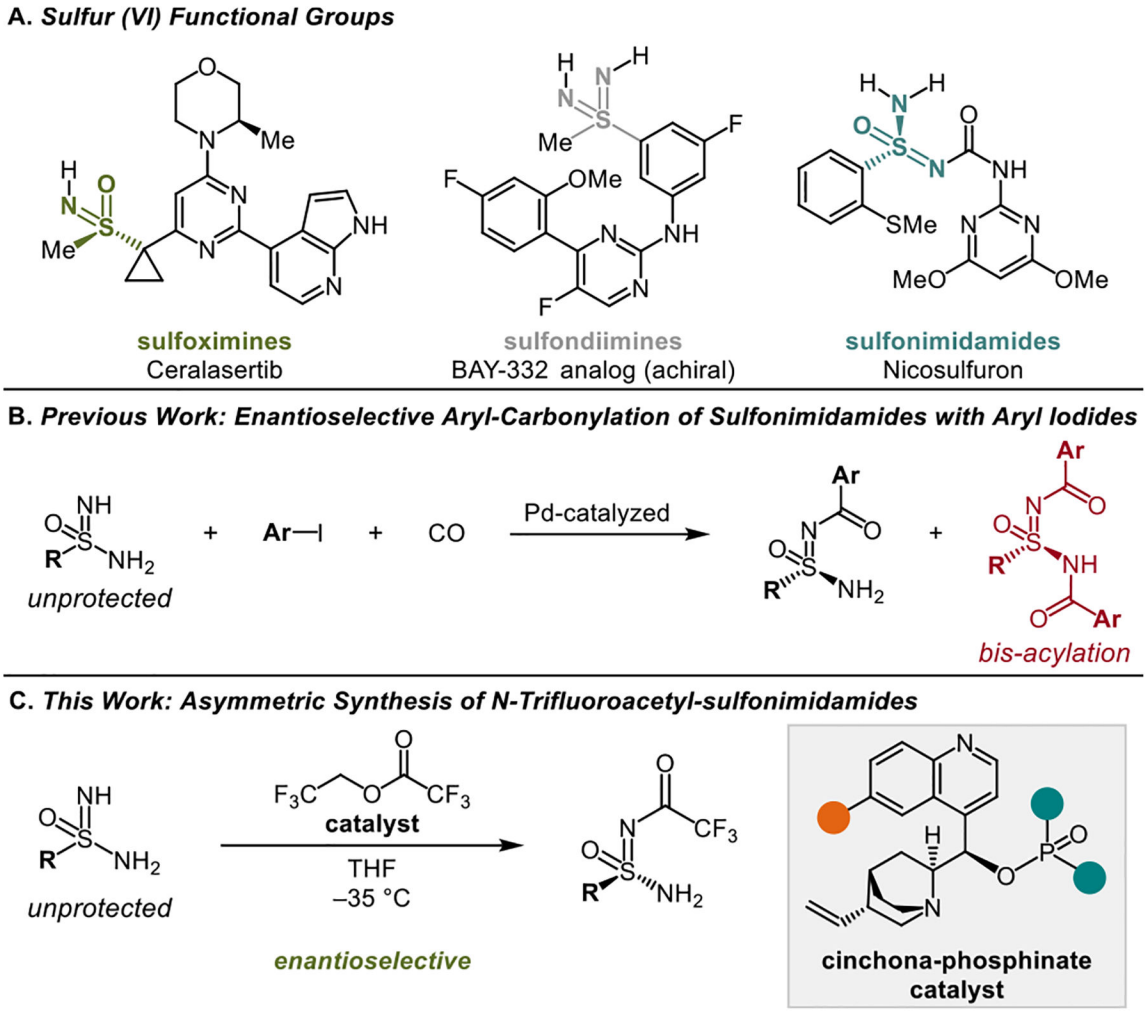

Figure 1.

(A) Medicinally relevant molecules containing sulfur(VI) functional groups. (B) Previously reported desymmetrization of sulfonimidamides. (C) This work.

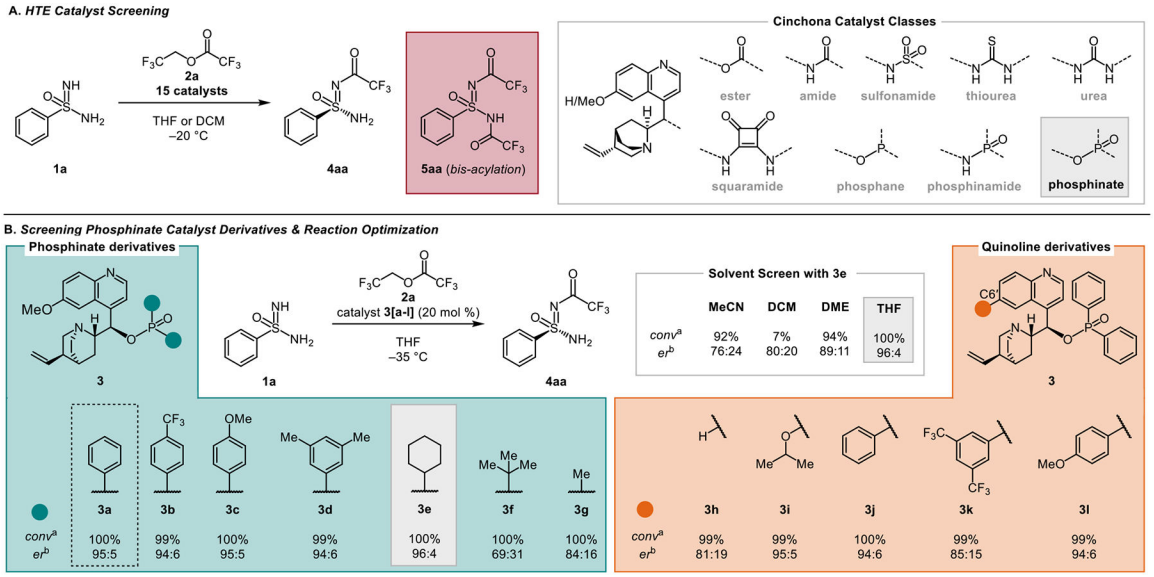

Figure 2.

(A) HTE screening of cinchona-derived catalysts to identify leads. (B) Optimization of cinchona-phosphinate catalysts and reaction solvent. Standard reaction conditions were as follows: **1a** (0.16 mmol, 1.0 equiv), **2a** (0.48 mmol, 3.0 equiv), and catalyst **3** (0.032 mmol, 20 mol %) in THF (3.2 mL, 0.05 M) at −35 °C. [a]Relative product area % as determined by SFC analysis. [b]Enantiomeric ratio (er) of product in the crude reaction mixture, as determined by chiral SFC analysis.

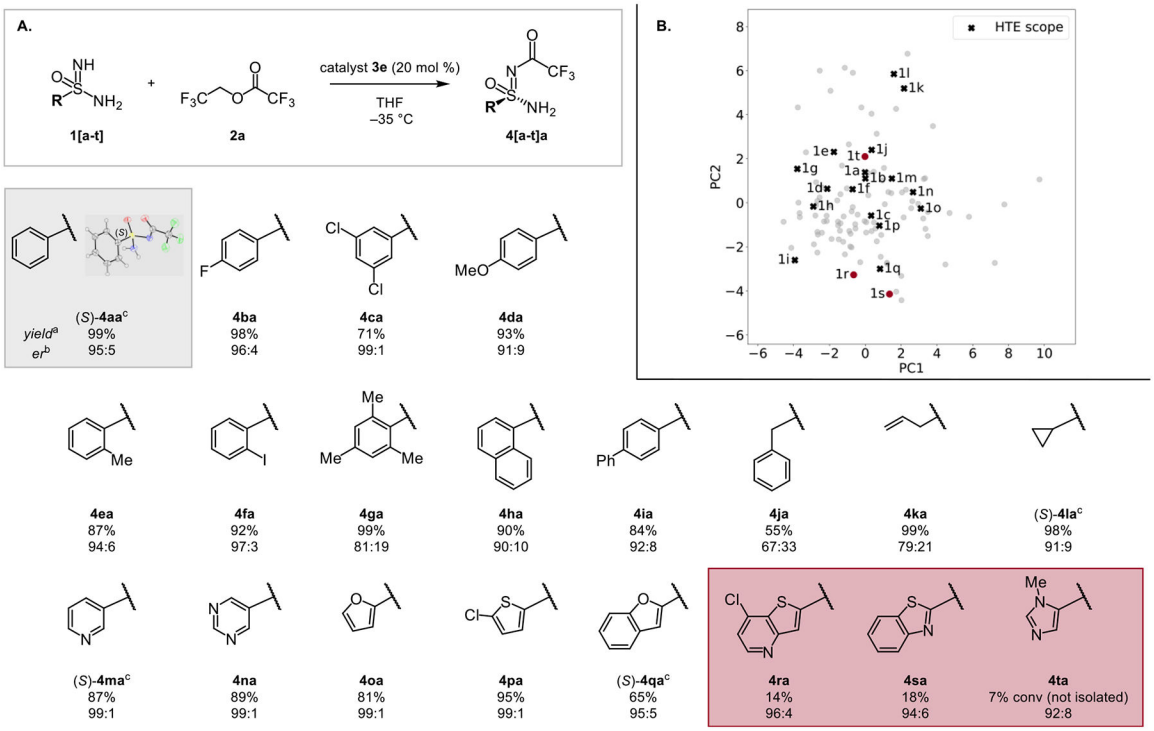

Figure 3.

Exploration of the sulfonimidamide substrate scope. (A) Sulfonimidamide substrate scope. Reaction conditions: substrate **1** (1.00 mmol, 1.0 equiv), **2a** (3.00 mmol, 3.0 equiv), and catalyst **3e** (0.20 mmol, 20 mol %) in THF (20.0 mL, 0.05 M) at −35 °C. [a]Isolated yield after purification. [b]er of the isolated product, as determined by chiral SFC analysis. [c]Absolute configuration was determined by X-ray crystallographic analysis. (B) PCA of synthetically feasible sulfonimidamides (43.5% of the total variance depicted with two principal components), selected substrates are labeled, and black crosses indicate substrates screened using HTE.

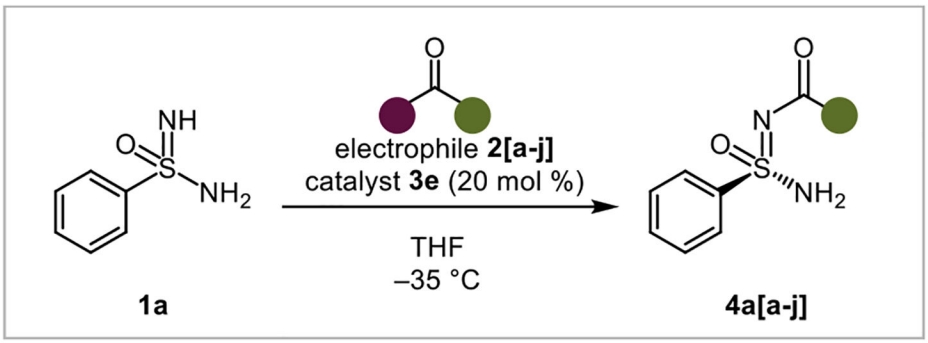

		conv[a]	er[b]			conv[a]	er[b]
2a	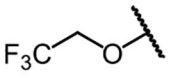	99%	96:4	2f	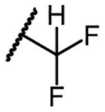	48%	99:1
2b	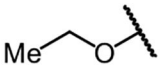	0%	n.a.	2g		0%	n.a.
2c	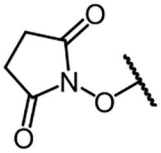	100%	50:50	2h		0%	n.a.
2d	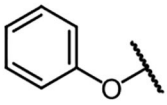	99%	52:48	2i	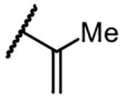	0%	n.a.
2e	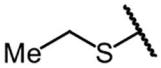	77%	77:23	2j	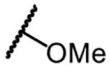	0%	n.a.

Figure 4.

Exploration of the electrophile scope. Reaction conditions: **1a** (0.16 mmol, 1.0 equiv), electrophile **2** (0.48 mmol, 3.0 equiv), and catalyst **3e** (0.032 mmol, 20 mol %) in THF (3.2 mL, 0.05 M) at −35 °C. [a]Relative product area % as determined by UPLC-MS/SFC analysis. [b]er of the product in the crude reaction mixture, as determined by chiral SFC analysis.

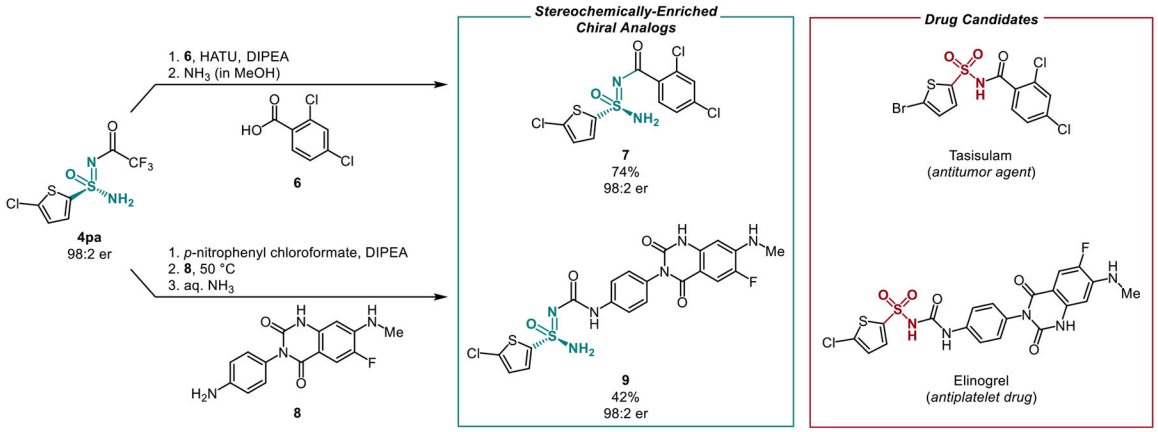

Figure 5.

Application of this methodology to synthesize chiral sulfonimidamide analogs of sulfonamide-containing drug candidates.

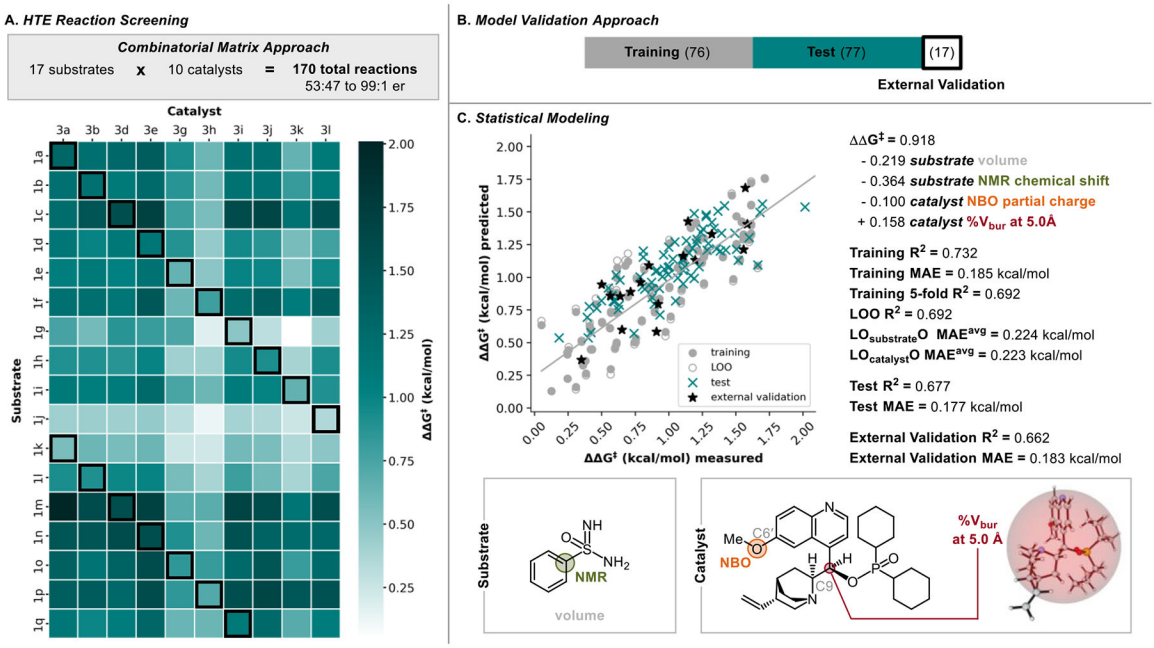

Figure 6.

Statistical modeling of the substrate catalyst relationship. (A) Employment of a combinatorial matrix approach for HTE screening of enantioselectivity for 17 sulfonimidamide substrates against 10 cinchona-phosphinate catalysts. (B) Data were curated for statistical model validation. (C) Multivariate linear regression (MLR) model for enantioselectivity built from Boltzmann averaged descriptors and depictions of the molecular descriptors included in the model. Computational method: M06-2X/def2-TZVP// B3LYP-D3BJ/6-31G(d,p).

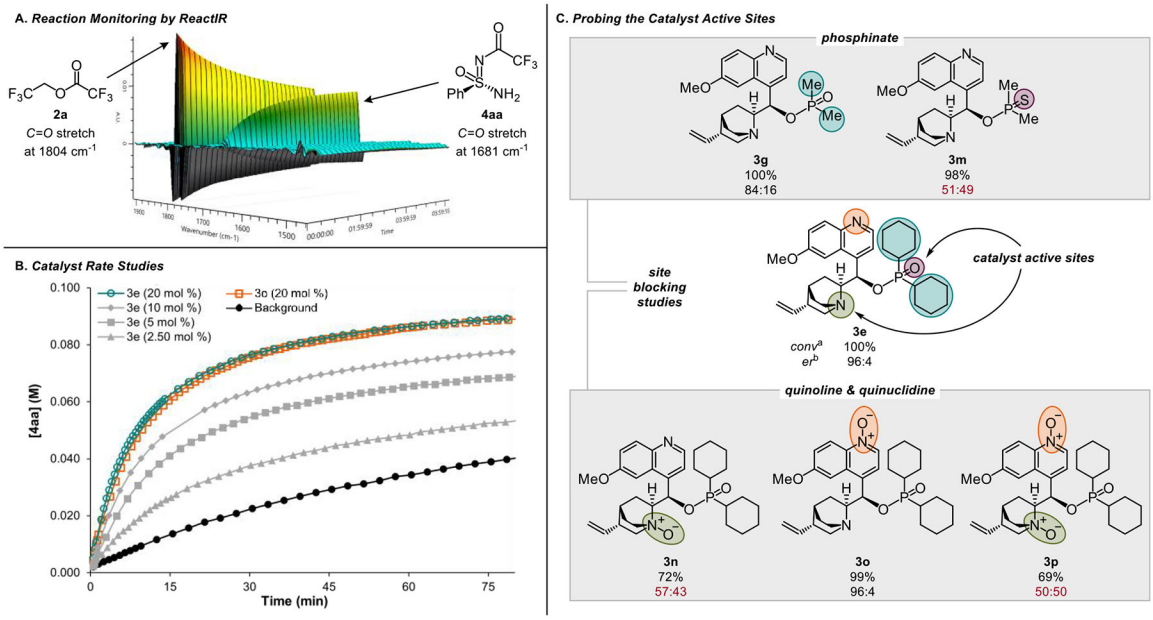

Figure 7.

Experimental mechanistic investigation results. (A) Carbonyl region from a ReactIR waterfall plot for the reaction of **1a** and **2a** with catalyst **3e** under the standard catalytic conditions, showing the conversion of **2a** and the formation of **4aa**. (B) Reaction profiles for a series of experiments using varying initial concentrations of catalyst **3e**, the quinoline *N*-oxide catalyst derivative **3o**, and the uncatalyzed background reaction. (C) Catalyst derivatives used to elucidate active site(s). Reaction conditions: **1a** (0.16 mmol, 1.0 equiv), **2a** (0.48 mmol, 3.0 equiv), and catalyst **3** (0.032 mmol, 20 mol %) in THF (3.2 mL, 0.05 M) at −35 °C. [a]Relative product area % determined by SFC analysis. [b]er of the product in the crude reaction mixture was determined by chiral SFC analysis.

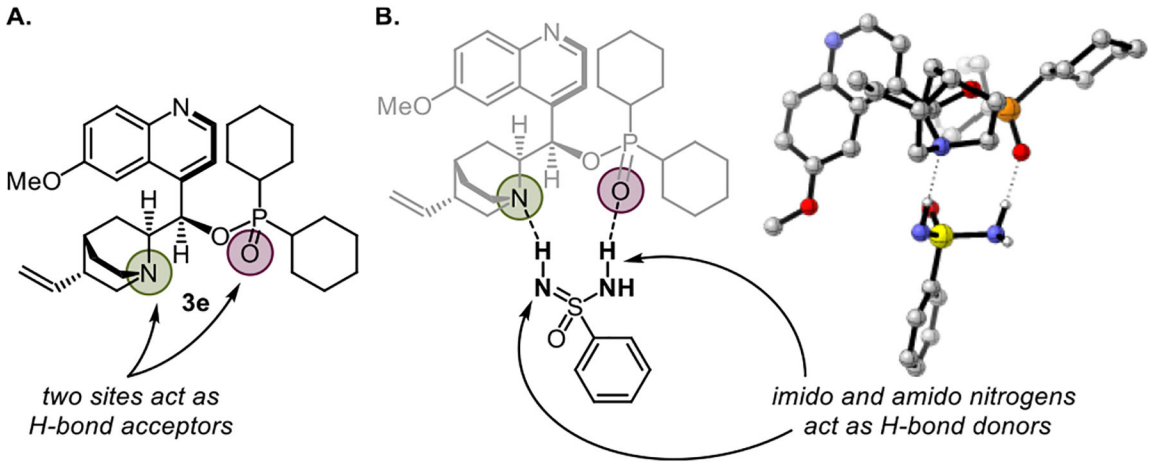

Figure 8.

Substrate-catalyst hydrogen-bonding interactions. (A) Hydrogen-bond acceptor sites on cinchona-phosphinate catalyst **3e**. (B) The schematic model and illustrative optimized structure showing the catalyst-substrate binding mode with two hydrogen-bonds.

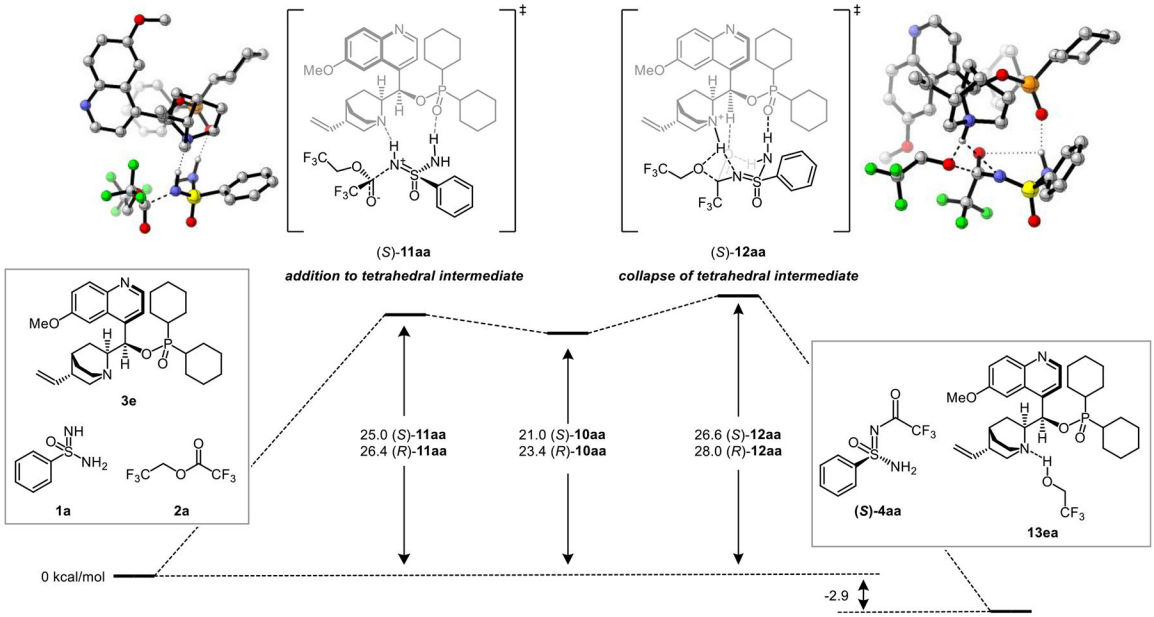

Figure 9.

Calculated transition state structures and energy barriers for tetrahedral intermediate formation and tetrahedral intermediate collapse. Computational method: ωB97XD/def2TZVPP (SMD(THF))//ωB97XD/def2SVP.

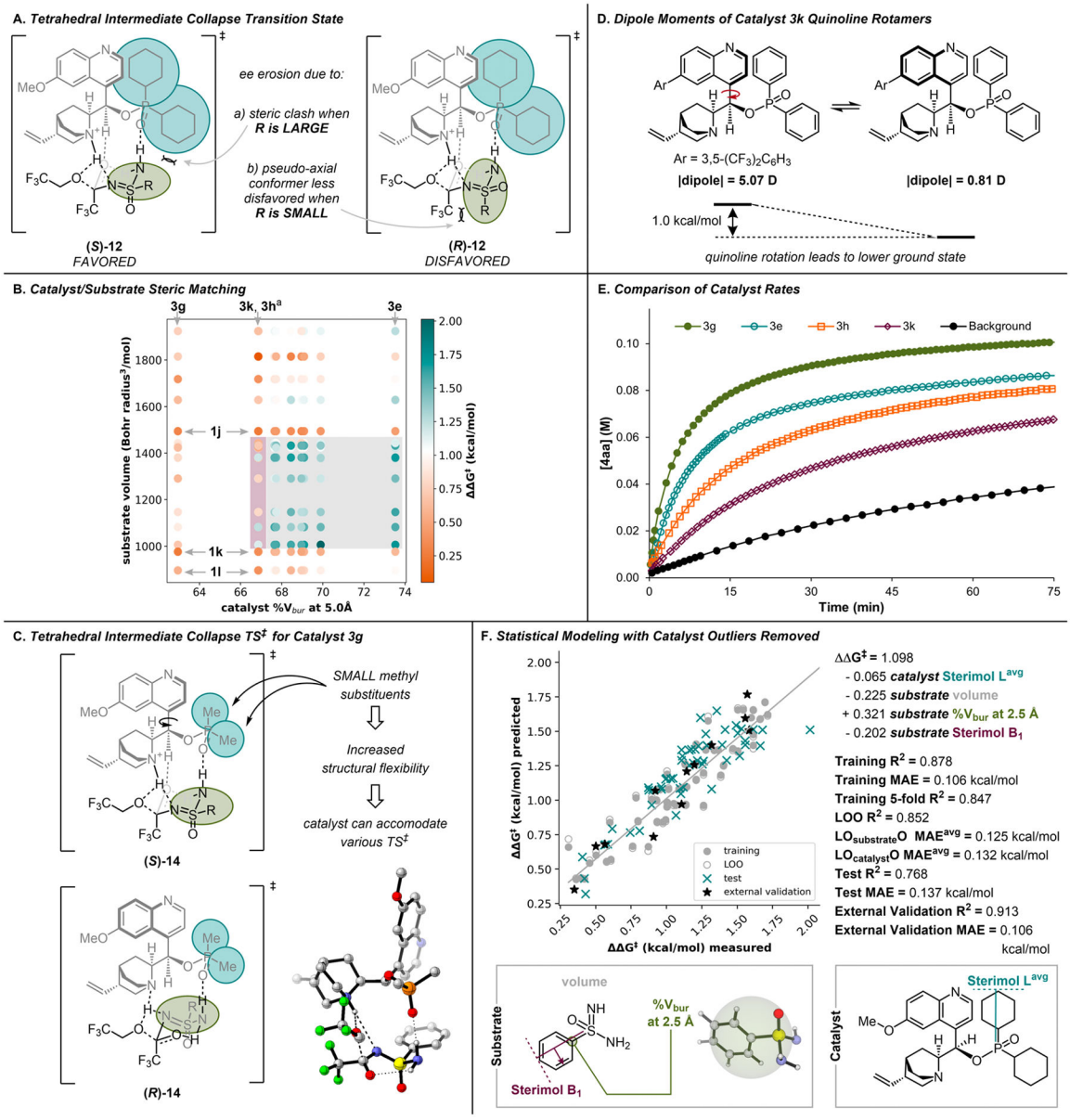

Figure 10.

(A) Tetrahedral intermediate collapse transition state structures of catalyst **3e** leading to the (*S*)-enantiomer and the (*R*)-enantiomer. (B) Substrate volume plotted against catalyst buried volume with the measured $\Delta\Delta G^{\ddagger}$ overlaid as a heatmap. The gray-shaded region indicates a high enantioselectivity. [a]Data points for catalysts **3k** and **3h** overlap in the plot because they have nearly the same $\%V_{bur}$. (C) Transition states for the tetrahedral intermediate collapse of catalyst **3g**. (D) Impact of quinoline rotamers of catalyst **3k** on the overall dipole moment and ground state energies. (E) Reaction profiles for various catalysts and the uncatalyzed background reaction. (F) MLR model for enantioselectivity trained without catalysts **3g, 3h**, and **3k** and depictions of the molecular descriptors from the lowest energy conformer

included in the model (12 reactions were used as external validation, and a Kennard Stone algorithm was used to split the remaining 107 reactions 50:50 into training:test sets).